Surface & Coatings Technology 494 (2024) 131449

Contents lists available at ScienceDirect

Surface & Coatings Technology

journal homepage: www.elsevier.com/locate/surfcoat

Corrosion resistance of HiPIMS tungsten and tungsten-aluminium coatings in contact with liquid Sn

D. Vavassori [a], L. Bana [a,*], M. Bugatti [a,b], G. Marra [c], V. Pinto [b], D. Dellasega [a,d], M. Iafrati [b], M. Passoni [a,d]

[a] Politecnico di Milano, Dipartimento di Energia, via G. Ponzio 34/3, Milano, Italy
[b] Department of Fusion and Technology for Nuclear Safety and Security, ENEA, Via E. Fermi 45, Frascati, Italy
[c] ENI S.p.A. Novara Laboratories (NOLAB), Renewable, New Energies and Materials Science Research Center (DE-R&D), via G. Fauser 4, 28100 Novara, Italy
[d] Istituto per la Scienza e Tecnologia dei Plasmi (ISTP) - CNR, via R. Cozzi 53, Milano, Italy

ARTICLE INFO

Keywords:
Liquid metal corrosion
Liquid tin
CuCrZr alloy
HiPIMS
Tungsten-based coatings
Morphology and microstructure characterization

ABSTRACT

Pure-tungsten and tungsten-aluminium films deposited by high power impulse magnetron sputtering (HiPIMS) on copper-chromium-zirconium substrates were investigated as protective coatings against liquid tin corrosion, a critical issue for nuclear fusion applications. The growth of pure-tungsten coatings was controlled by using a negative substrate bias synchronized to the HiPIMS pulse onset, resulting in columnar films with various degree of compactness and crystallinity according to the set bias amplitude (0, 400 and 800 V). Differently, the co-sputtering of W and Al favored the formation of an amorphous layer with a compact morphology. During liquid tin corrosion experiments at 400 °C for up to 600 min, all produced coatings were not dissolved, but different protective performances were observed after localized liquid tin interaction. Pure-W coated samples suffered from tin penetration after brittle failure of the protective layer. On the contrary, under the same experimental condition, W—Al coatings proved to be effective in limiting liquid tin attack.

1. Introduction

In the last decades, liquid metals (LMs) have gained interests for several applications related to energy production and storage [1–3]. As far as nuclear power is regarded, LMs are considered a key technology to develop future systems thanks to their advantageous thermophysical properties [4–6]. Specifically, lead (Pb) and lead-bismuth eutectic (LBE) are promising coolants for the realization of generation IV fission reactors [7]. In the context of magnetic confinement fusion research, lithium (Li), gallium (Ga) and tin (Sn) are considered for non-conventional designs of the divertor which is a crucial component for the dissipation of the intense heat and particles fluxes generated by nuclear fusion reactions [8–10]. However, the susceptibility of most structural materials to LM corrosion is a critical issue to be tackled to ensure the integrity of the components. Thus, the investigation of the interaction between LMs and materials and the identification of strategies for the mitigation of corrosion phenomena represent fundamental research areas. This especially applies if the aim is the integration of LMs in a nuclear environment which, being characterized by high temperatures and strong radiation fields, introduces constraints on the choice of possible structural materials.

In this framework, the development of LM-based divertor concepts is worth of consideration as an alternative to solid tungsten (W)-based divertor [11,12]. The most mature designs are based on a Capillary Porous System (CPS) constituted by a porous mesh that exploits capillarity to confine the LM [13]. Generally, the soaked CPS is placed directly in contact with the cooling pipes that, to satisfy the thermo-mechanical requirements imposed by the fusion power flux, are made of copper-chromium-zirconium (CuCrZr) alloy [9,10]. Among low-melting point metals, Sn is considered a promising candidate thanks to its good thermal conductivity, high boiling point and low vapor pressure [8,14,15]. However, significant liquid Sn corrosion is expected on Cu-based materials, even at the intermediate operating temperature of the nuclear fusion components (~ 400 °C) [10]. Indeed, studies developed in the microelectronics sector showed that the interaction between liquid Sn and solid Cu proceeds by a rapid Cu dissolution in Sn, leading to the nucleation of the hexagonal η phase (Cu_6Sn_5) and the orthorhombic ε phase (Cu_3Sn) [16–22]. Typically, the latter phase grows as a

* Corresponding author.
E-mail address: luigi.bana@polimi.it (L. Bana).

https://doi.org/10.1016/j.surfcoat.2024.131449
Received 30 July 2024; Received in revised form 5 October 2024; Accepted 7 October 2024
Available online 11 October 2024

thin layer close to the Cu surface, while the former expands towards Sn exhibiting a peculiar scallop-like morphology [23]. Even if the formation of these InterMetallic Compounds (IMCs) at the Cu—Sn interface progressively slows the process, their growth in a realistic component would severely compromise its thermal and mechanical performance.

To avoid LM corrosion, the presence of protective coatings represents a possible solution. In the context of nuclear energy systems, coatings composed by metallic alloys or ceramics have been comprehensively investigated for fast fission reactors demonstrating to be an appealing option to improve components resistance against Pb and LBE corrosion [24–29]. On the contrary, the literature is quite scarce regarding the mitigation of liquid Sn corrosion. In the last years, different classes of materials were tested in corrosion experiments involving liquid Sn. Nevertheless, only a limited number of refractory metals and ceramics (e.g., tungsten, molybdenum, silicon carbide or alumina) demonstrated to be inert concerning their bulk form. [14,30–36]. Considering the long-lasting experience on W-coatings in a fusion environment [37–39] and its wettability in liquid Sn [35], W and its alloys candidate as barrier layer material. Interestingly, a recent work [40] related to applications in electronics and soldering reported an enhancement in the control of the interaction between liquid Sn and a Cu substrate covered with a nickel layer alloyed with molybdenum (Mo). However, for CuCrZr bulk no investigation has been yet performed on the development and behaviour of a corrosion barrier against liquid Sn concerning the previously described LM-based divertor design.

In this respect, the fine tailoring of coating properties at the nanoscale represents a key aspect to optimize the performances in the harsh LM environment. To this end, the choice of advanced deposition methods can be beneficial. Specifically, among the Physical Vapor Deposition (PVD) family, High Power Impulse Magnetron Sputtering (HiPIMS) [41] is noteworthy. HiPIMS builds upon the working principles of Direct Current Magnetron Sputtering (DCMS) but, instead of a constant negative voltage, high amplitude voltage pulses (10s–100s μs long) are applied to sputter the material cathode. This leads to peak power densities in the range 0.5–10 kW/cm^2, usually two orders of magnitude larger than the time-averaged values. As a result, a high density plasma (10^{18}–10^{19} m^{-3}) characterized by a significant fraction of ionized sputtered species is generated. The presence of ions of the deposited material opens new ways to engineer films with controlled morphology, microstructure and adhesion. Indeed, the application of proper electric fields (e.g., a substrate bias voltage) allows to tune the trajectory and energy of the ionized sputtered species, influencing the film growth dynamics [42–44]. Specifically, considering the W HiPIMS discharge, recent works [45–48] reported the deposition of films exhibiting superior quality in terms of structural, mechanical and tribological properties if compared to films obtained by the more conventional DCMS. Moreover, as reported in previous works [49–51], the co-sputtering of refractory metals (W or Mo) with other metallic materials such as aluminium (Al) can be adopted as complementary strategy to properly modify coating characteristics (e.g., moving from a solid solution phase to an amorphous-like one).

This work aims at evaluating W and W—Al films with different morphological and microstructural properties as protective layers on CuCrZr component against liquid Sn corrosion. Considering a 100 μs long HiPIMS pulse, depositions of films via sputtering from a single W target and via co-sputtering from a W target and an Al target were investigated to coat planar CuCrZr substrates. In the former case, both unbiased conditions and the application at substrate of 100 μs long negative bias pulses synchronized with the HiPIMS pulse onset (bias voltage delay $\Delta\tau = 0$ μs) and with amplitude (U_S) of 400 V and 800 V were considered. In the latter case, both cathodes were powered in HiPIMS mode to fully exploit a highly ionized and energetic plasma environment favoring the formation of a compact and uniform coating on an uncommon substrate as the CuCrZr one. The produced samples were tested in corrosion experiments exploiting the static droplet approach [21,40,52–56] at 400 °C for relatively short periods of time (150 or 600 min). While shorter than the expected divertor lifetime, these exposure times allow for the investigation of the barrier effectiveness on the most relevant time-scales, given the fast chemical interaction between Cu and Sn. Morphology, microstructure and composition of the coatings were characterized before and after the exposure. In light of these analyses, the protective performances against liquid Sn corrosion are discussed.

2. Experimental methods

2.1. Coatings deposition

Planar CuCrZr substrates were machined from commercial-grade bulk material. All substrates presented a squared or rectangular shape (10–25 mm in length and in width), while the thickness was varied in the 1–10 mm range. Specifically, the minimum thickness was constrained taking into account the solubility limit of Cu into molten Sn at 400 °C of around 13 at.% [57]. Following the assumption of homogeneous dissolution over the whole contact area (for more details see paragraph 2.3) and no intermetallic compound formation, a dissolved substrate thickness of about 0.2 mm would result. However, both the formation of Cu—Sn IMCs and possible localized corrosive attack would lead to a larger penetrated thickness. The minimum thickness of 1 mm was therefore chosen as a conservative value to avoid a complete Sn penetration through the substrate.

The substrates were grinded with SiC paper (up to 2500 grit) and, successively, mechanically polished (3 μm diamond finishing). Surface oxides and impurities were removed using proper metal-cleaning agents. The samples were immersed in a solution composed by anionic and non-ionic surfactants for a few minutes. Once extracted, solution residues on samples surface were removed by water. Finally, samples were rinsed using isopropanol.

Two kind of coatings were deposited: pure tungsten (W) and tungsten aluminium (W—Al). Films were grown onto the above described CuCrZr substrates and, for morphology and structure analyses, onto single side polished 500 μm thick (100) silicon wafers cleaned using isopropanol. In all cases, prior to coating deposition, the vacuum chamber was pumped to a base pressure lower than 5×10^{-4} Pa. Argon (99.999 % purity) working pressure was fixed to 0.5 Pa and the inlet gas flow to 40 sccm. Concerning the magnetron sputtering system described in [43], the targets to substrate distance was set to 16 cm. Targets were inclined of 18° with respect to the substrate normal. To ensure deposition uniformity, the sample holder was rotated at a uniform speed of 5 rpm in all cases. The sample holder was not intentionally heated during the process. For pure-W films, one cathode was equipped with a circular W target (diameter = 76 mm, thickness = 6 mm) and a dual-channel SIPP2000 generator (Melec GmbH, Germany) was used to power it in the HiPIMS process. The HiPIMS pulse length, duty cycle and frequency were set to 100 μs, 1.75 % and 175 Hz.

The average power was fixed to 230 W, corresponding to a peak power density and peak current density of about 0.6–0.7 kW/cm^2 and 0.9–1 A/cm^2, respectively.

During the deposition, the application to the substrate of 100 μs long negative bias pulses synchronized with the HiPIMS pulse onset (bias voltage delay $\Delta\tau = 0$ μs) was considered. The described bias configuration was selected relying on a previous study [48] focused on the morphology, structural and residual stress characterization of HiPIMS W films deposited in similar bias conditions. Before the deposition of each coating, a pure-W "bottom layer" was realized setting U_S equal to 800 V. The deposition time for the "bottom layer" was set to 20 min to achieve a thickness of 100 nm. It is worth mentioning that this layer is essential to guarantee a satisfactory adhesion of the coating on the CuCrZr substrate. Indeed, the direct growth of W-based coatings without bias application or with the application of lower amplitude pulsed bias led to a poor adhesion on the CuCrZr substrate. Subsequently, the bias voltage was adjusted to the desired amplitude until the end of the process. According

to the applied bias amplitude the total deposition time was set to 80 min ($U_S = 0$ V), 95 min ($U_S = 400$ V), 110 min ($U_S = 800$ V) to obtain in all cases a film thickness around 400–500 nm. Hereinafter, W-0 will refer to the pure-W coating deposited setting $U_S = 0$ V, W-400 to the one deposited setting $U_S = 400$ V and W-800 to the one deposited setting $U_S = 800$ V.

W—Al coatings were produced by simultaneously co-sputtering a W and an Al sources. For this purpose, a second cathode was equipped with an Al target (diameter = 76 mm, thickness = 6 mm). Also in this case, the dual-channel SIPP2000 generator was used to power the cathodes in the HiPIMS process. Concerning the W target, the sputtering configuration described for the production of W-0 films was used. To sputter the Al target, the same HiPIMS pulse parameters adopted for the W target were selected, but fixing the average power to the nearly constant value of 380 W. This corresponded to a peak power density and peak current density of about 0.9–1 kW/cm^2 and 1.4–1.5 A/cm^2, respectively. Before the co-deposition, as in the pure-W coatings case, the deposition of the above described "bottom layer" was considered. In addition, to improve the wettability of liquid Sn on the coating, a "top layer" with equal characteristics was added, thus leading to the formation of a pure-*W*/W-Al/pure-W sandwich structure. The total deposition time was set to 85 min to obtain a film thickness of approximately 700–800 nm. Table 1 resumes the applied process parameters for film deposition on CuCrZr substrates. Moreover, one set of co-deposited coatings was realized on (100) silicon substrates without adding the "top layer" to perform a proper compositional and microstructural analysis of the W—Al layer only. This set of sample was not considered for corrosion tests.

2.2. Coatings characterization

The morphological properties of coatings before and after corrosion experiments were investigated using a LEICA DMI5000 M inverted optical microscope and a Zeiss Supra 40 field emission Scanning Electron Microscopy (SEM) operating at an accelerating voltage of 5 kV.

To perform elemental analysis, Energy Dispersive X-ray Spectroscopy (EDX) was performed coupling the SEM apparatus whit a Xplore 15 EDS detector (Oxford Instruments) and setting the accelerating voltage to 15 kV. Specifically, to cross-sectionally characterize the interaction region with the LM, samples were embedded in the two-component epoxy resin Technovit 5017 (Kulzer, GmbH, Hanau, Germany), cutted using a silicon carbide rotating blade, polished and cleaned with ethanol.

The crystalline phase and crystallographic orientation of the coatings grown on CuCrZr substrates was evaluated through X-Ray Diffraction (XRD) analysis performed by a Rigaku Geigerflex diffractometer with a Cu-Kα source, working in θ-2θ configuration. Moreover, additional grazing incidence X-ray diffraction (GIXRD) measurements were performed on W-800 and W—Al coatings deposited on Si substrates using a Panalytical X'Pert Alpha-1 diffractometer with a Cu-Kα source and setting ω equal to 1.0°. Specifically, for this analysis the set of W—Al samples without the "top layer" were considered.

Table 1
Discharge parameters considered for films deposition on CuCrZr substrates.

Sputtered cathode	pure-W	W-Al
	Tungsten	Tungsten, aluminium
Ar Pressure [Pa]	0.5	0.5
Pulse Length [μs]	100	100, 100
Frequency [Hz]	175	175, 175
Duty Cycle [%]	1.75	1.75, 1.75
Discharge Voltage [V]	690–740	690–740, 650–700
Average Discharge Power [W]	230	230, 380
Peak Current Density [A/cm^2]	0.9–1	0.9–1, 1.4–1.5
Bias Voltage Amplitude [V]	0, 400, 800	0
Bias Voltage Delay [μs]	0	–
Deposition Time [min]	80[a], 95[a], 110[a]	85[a]
"Bottom layer"	Yes	Yes
"Top layer"	No	Yes

[a] The deposition of "bottom" and/or "top" layers is included. The deposition of a single layer requires ~ 20 min.

2.3. Corrosion tests

Corrosion tests were performed in a resistive vacuum oven installed at ENEA-Centro Ricerche Frascati (Italy). About 1.5 ± 0.1 g of Sn (99 % purity) was positioned on top of each sample and surrounded by an alumina tube (diameter = 10 mm) in order to keep constant the interaction area throughout the experiments. Then, samples were inserted into an alumina crucible and positioned in the lower part of the oven. A K-type termocouple directly in contact with the base of the samples was exploited to monitor the temperature. Before experiments, the oven chamber was evacuated down to a background pressure of 5×10^{-3} Pa monitored through a full-range pressure gauge. A heating cycle characterized by a temperature increase of 5 °C/min was applied until the desired temperature of 400 °C was reached. The temperature was kept constant during the whole experiment duration, equal to 150 or 600 min. Subsequently, the system was slowly cooled to 50 °C before venting the chamber and extracting the samples.

3. Result and discussion

3.1. Coatings deposition and characterization

3.1.1. HiPIMS waveforms

For the W and Al targets, Fig. 1(a) and (b) exemplify typical experimental HiPIMS discharge voltage and current waveforms acquired during deposition on CuCrZr substrates. Moreover, Fig. 1(a) also reports the characteristics of the three different pulsed bias voltages applied to the substrate and synchronized with the HiPIMS pulse onset considered for the deposition of pure-W coatings. For both materials, the discharge voltage waveform is approximately constant during the pulse on-time, resulting in a rectangular shape. The temporal evolution of the discharge current density related to the W target presents a peak value of about 1 A/cm^2 (t ≈ 40 μs) and, successively, decreases down to approximately 0.7 A/cm^2 as a consequence of the strong working gas rarefaction promoted by the sputtering of heavy elements like W [47]. Differently, the discharge current waveform of the Al target shows a more pronounced increase up to 1.4–1.5 A/cm^2 and remains constant at this value until the end of the pulse. The two described behaviours suggests that the HiPIMS discharge mode is different for the two metals. Probably, for the W discharge a mixed working gas sputtering and self-sputtering regime can be assumed, while the self-sputtering regime plays a major role during the Al discharge [47,48,58].

3.1.2. Morphology characterization

Fig. 2 displays the morphological properties of the produced W-based coatings. The first column (Fig. 2(a-e)) and the second column (Fig. 2(f-l)) report the SEM cross sectional and planar micrographs of coatings deposited on silicon substrates. The third column (Fig. 2(m-q)) reports the planar SEM micrographs of the coatings deposited on CuCrZr substrates. All pure-W coatings present a columnar growth up to a thickness of approximately 400 nm. Specifically, the W-0 coating presents the narrowest columns (Fig. 2(a)), resulting in a nano-ridged superficial pattern exhibiting well-defined streaked and rippled features (Fig. 2(f)). The same structures are also visible considering the coating deposited on the CuCrZr substrate (Fig. 2(m)). The introduction of the bias voltage during coating depositions leads to a morphology variation. SEM micrographs of fracture cross sections (see Fig. 2 (b) and (c)) show a progressive widening of columns size. As explained in previous studies about W HiPIMS films [47,48], the high energy of the ionized species selectively accelerated towards the substrate by the pulsed bias favors thermally induced

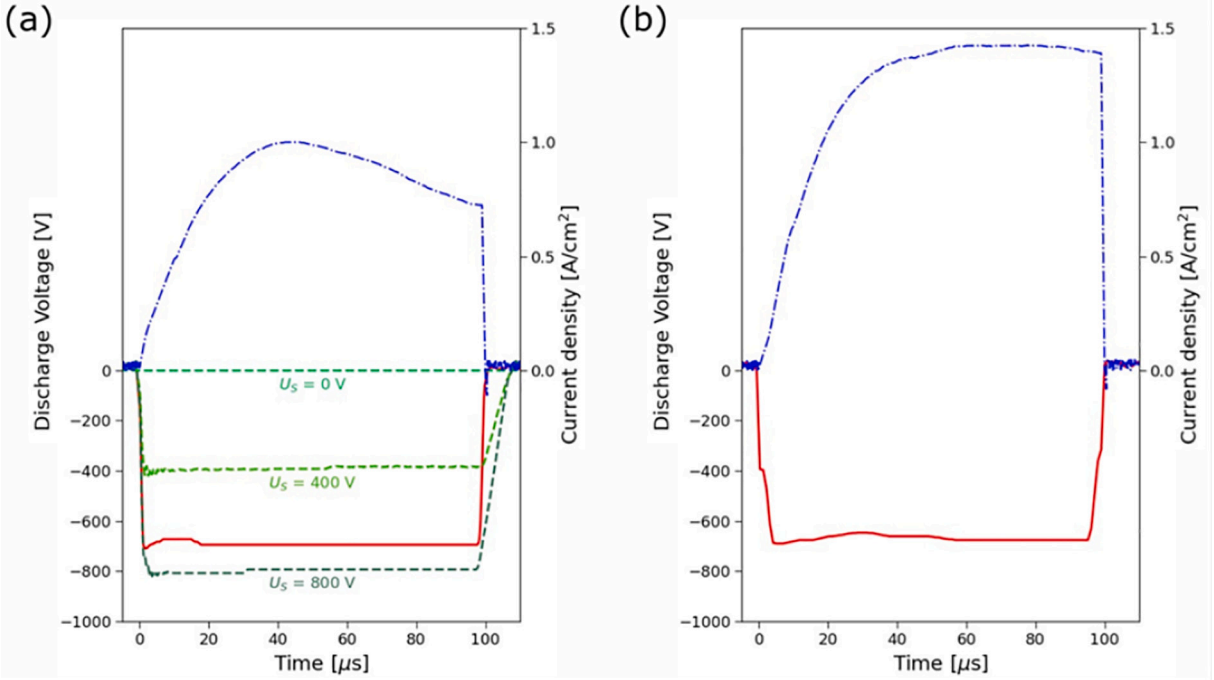

Fig. 1. Temporal evolution of the discharge voltage (red) and current density (blue) waveforms acquired for the (a) W target and (b) Al target. In panel (a) the bias voltage waveforms (green) synchronized with the HiPIMS pulse onset related to the deposition of pure-W coatings are also reported.

processes (e.g., defects annealing or diffusion and release of trapped argon gas atoms). This promotes an enhanced grain boundary motion and, in turn, grain coarsening and increase of columns size. As a consequence, on both Si and CuCrZr substrates, the coatings top-surface (see Fig. 2(g-h) and (n-o)) appears more homogeneous. Indeed, the nano-ridged pattern observed for the W-0 coating is hardly recognizable, probably also due to re-sputtering effect caused by the dramatic increase of the bombarding ion energy. It is important to note that in all pure-W coatings the presence of the 100 nm thick"bottom layer", is not easily identifiable. Indeed, if on one side its presence is crucial to guarantee films adhesion on the metallic substrate, on the other it does not heavily influence the subsequent coating growth in terms of morphology, which is rather governed by the specific bias voltage configuration adopted.

A different morphology can be appreciated for the W—Al coatings. On the one hand, the cross-section SEM image (Fig. 2(d)) clearly evidences the three constituents of the coating: the pure-W "bottom" and "top" layers (approximately 100 nm in thickness each) and the central one produced by the co-deposition of W and Al (approximately 600 nm in thickness). This latter layer is characterized by a featureless growth which leads to a compact and dense morphology. On the other hand, due to the presence of the"top layer", the features of the coating surface resemble the ones described for the W-800 coating (see Fig. 2(i) and (p)). To precisely retrieve the chemical composition of the W—Al layer, the corresponding set of samples realized without the"top layer" has been considered. The morphology of these samples is displayed in Fig. 2 (e), (l) and (q). The cross-section is similar to the one shown in Fig. 2(d), but in the upper part of the coating a brighter region corresponding to a "folded layer", typically exhibited by metallic glass films after fracture [59,60], is visible. Instead, planar SEM images result different due to the absence of the "top" layer. On Si substrate, film morphology results uniform and featureless (see Fig. 2(l)). The coating exhibits the same characteristics also on CuCrZr (see Fig. 2(q)), but some features related to the metallic substrate irregularities can be recognized. The EDX investigation on these samples proved equi-atomic mixture of W and Al in the coating (50 at.% W and 50 at.% Al), homogeneously over the sample surface, and a negligible fraction of impurities (e.g, oxygen or carbon). More details about the choice of this composition for the W—Al layer can be found in the "Supplementary Material".

3.1.3. Structural analysis

Fig. 3 reports the results related to the XRD measurements. Fig. 3(a) shows the diffractograms related to W-based films deposited on CuCrZr substrates. By comparing the patterns of the coated samples and the reference one (i.e., bare substrate), it is evident that all the analysed samples exhibit the contribution of the polycrystalline substrate. Specifically, four characteristic peaks of Cu (2θ = 43.316° (111), 50.449° (200), 74.125° (220) and 89.936° (311)) are visible. Concerning the pure W coatings, diffractograms indicate a dominant α-W structure (A2 bcc) with a ⟨110⟩ out-of-plane preferred orientation compatible with the previously described columnar growth. No peaks related to other orientations of this W phase were detected using the θ-2θ configuration. In all cases, the peak associated with the (110) reflection is centered at a 2θ angle lower than the reference position (2θ = 40.265° [47]) suggesting the presence of an intrinsic compressive stress state which relaxes as the applied bias voltage amplitude is increased, in agreement with previous findings on Si substrates [47,48]. A magnification of previous patterns restricted to the region around the α-W (110) peak (2θ = 37–45°) is displayed in Fig. 3(b). Focusing on the W-0 coated sample, its pattern reveals a slightly asymmetric α-W (110) peak. Differently, asymmetry does not characterize the α-W (110) peak exhibited by the diffractograms associated to samples realized with biased depositions. On the one hand, the bias amplitude U_S = 400 V seems to favors a better crystallization and orientation degree of the coatings with respect to the unbiased case. The main diffraction peak is centered at 2θ = 40.10°, resulting in a crystallite size (estimated with Scherrer formula) and an out-of-plane lattice parameter of approximately 18 nm and 0.318 nm, respectively. On the other hand, the intense bombardment promoted at U_S = 800 V enhances the distortion of the lattice coherence leading to a reduced crystalline quality, with a decrease in grain size down to around 14 nm and an out -of-plane lattice parameter of 0.317 nm.

Fig. 3(a) and (b) also depict the pattern related to W—Al coatings. It stands out that no peaks related to a pure Al phase were present and, similarly, no peaks associated with intermetallic phases were detected, despite the formation of IMCs is foreseen by the W—Al phase diagram

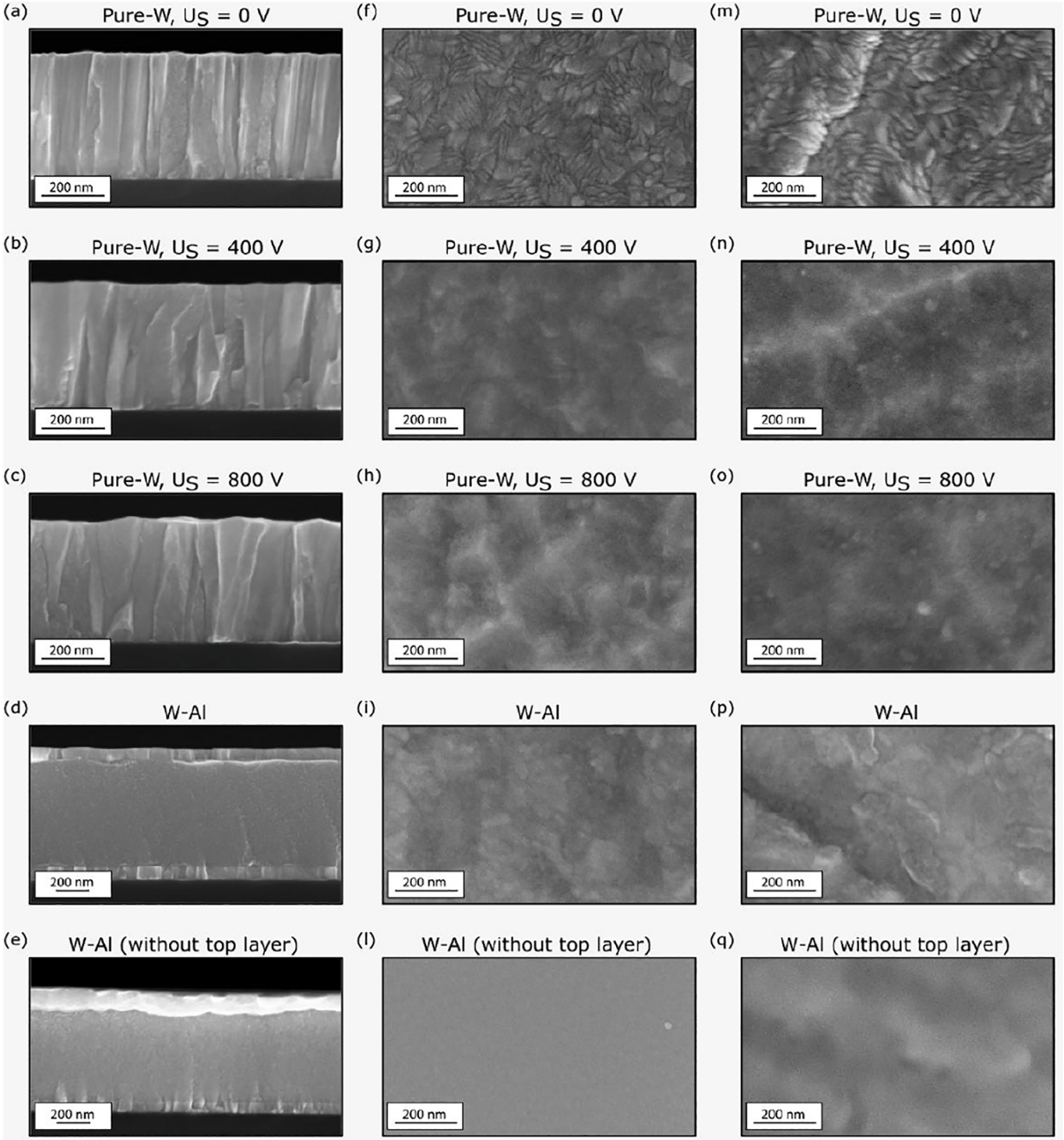

Fig. 2. SEM cross sectional micrographs of (a-c) pure-W, (d) W—Al coatings with "top" layer and (e) W—Al coatings without "top" layer deposited on a silicon substrate. SEM planar micrographs of pure-W and W—Al coatings deposited on (f-l) a silicon substrate and (m-q) a CuCrZr substrate.

for an equiatomic mixture of W and Al [61]. On the contrary, the W—Al diffractogram shows a peak around $2\theta = 40°$ that can be attributed to the α-W structure and that could be interpreted hypothesizing the formation of a solid solution of Al in W. However, it must be emphasized that the"top" and"bottom" layers constituting the"sandwich" structure of the W—Al coating can significantly contribute to this diffracted signal. In this framework, an interesting suggestion can be inferred from the signal-to-noise ratio characterizing the W—Al pattern. If compared to the one of W-800 coating, the signal-to-noise ratio of the W—Al pattern is lower indicating a reduced degree of cristallinity. Furthermore, while in the W-800 pattern the α-W (110) peak can be fitted with a single PseudoVoigt function superimposed on a linear background (see Fig. 3 (b.1)), fitting the same peak in the W—Al diffractogram requires the addition of a Gaussian contribution, centered at $2\theta \simeq 40.5°$ (see Fig. 3 (b.2)). These differences suggest a more complex structure of the W—Al coating. To further clarify this aspect, GIXRD measurements were performed to precisely characterize the microstructural properties of the W—Al layer only. To this end, the W—Al set of samples realized without

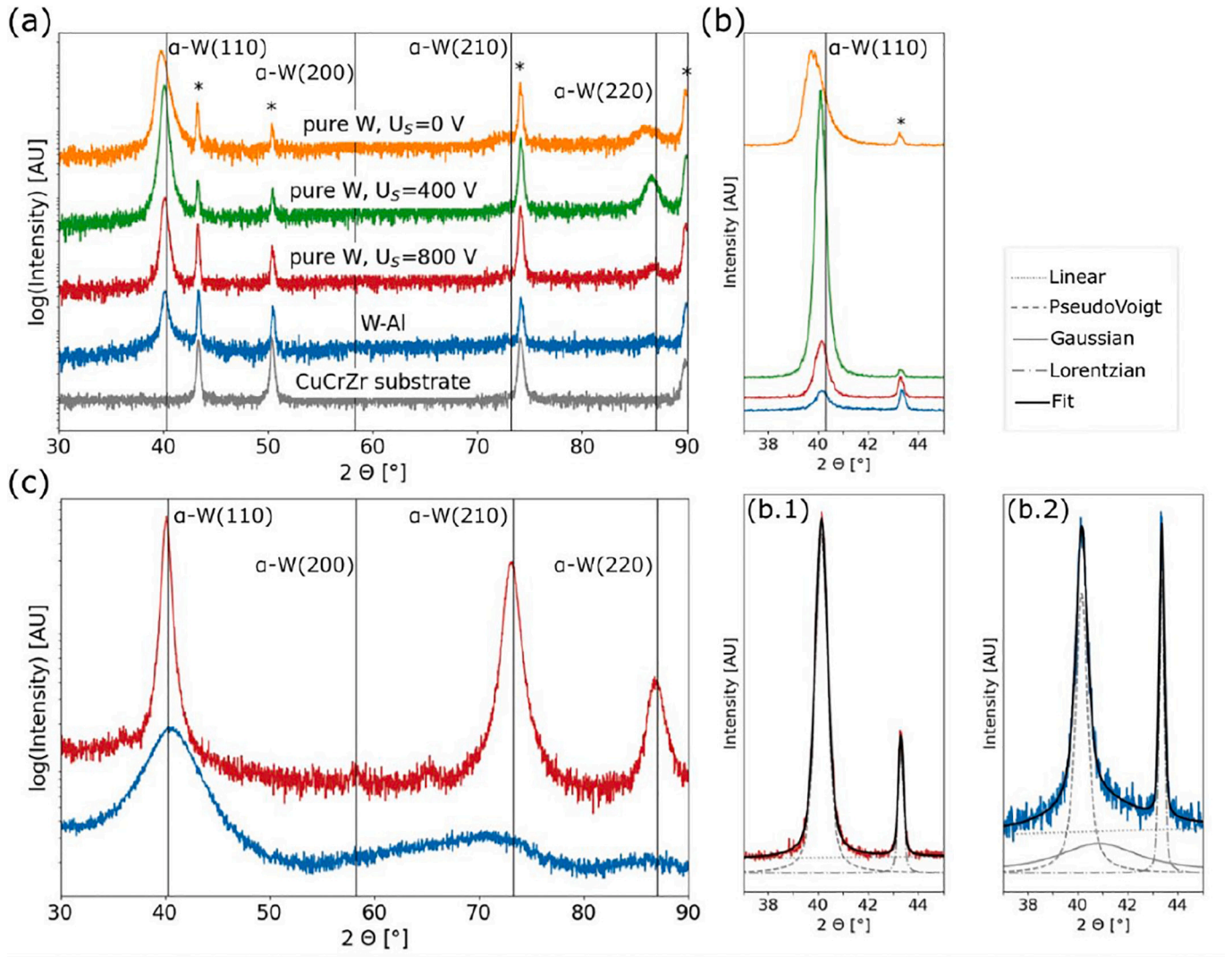

Fig. 3. X-ray diffractograms of the W-based coatings. (a) XRD patterns of pure-W and W—Al coatings deposited on CuCrZr substrates acquired with the θ-2θ configuration. The signal of the substrate is reported as a reference and the corresponding peaks are identified by (*). (b) Magnification of XRD patterns acquired with the θ-2θ configuration. The x-axis is restricted to the region $2\theta = 37–45°$. The curves related to (b.1) W-800 and (b.2) W—Al coatings have been studied using a fitting procedure. The legend refers to both panel (b.1) and (b.2). (c) GIXRD patterns of W-800 (red) and W—Al (blue) coatings deposited on Si substrates. The investigated W—Al coatings have been realized without the"top" W layer for a proper analysis of the mixed layer only.

the"top layer" was examined. For proper comparison, the same investigation was performed on W-800 coatings. The results of this analysis are shown in Fig. 3(c). If compared to the pattern acquired using the θ-2θ configuration (see Fig. 3(a)), the signal of the W-800 coating presents more than one peak related to the α-W structure, as widely reported for textured films. Indeed, in addition to the sharp α-W (110) peak, also the peaks related to the (211), (200) and (220) reflections are visibile at $2\theta = 58.26°$, 73.19° and 87.01°. Nevertheless, the (110) peak remains the most intense one, further supporting that the preferential growth of pure-W coatings is along the ⟨110⟩ direction.

A different behaviour characterizes the pattern of the W—Al layer. Firstly, it presents a wide gaussian peak centred at $2\theta \approx 40.5°$, corresponding to a d-spacing similar to the one between the (110) α-W planes, but widened and with a much lower intensity compared to the W-800 coating. This could explain the need of an additional Gaussian contribution in the previously discussed fitting procedure of the θ-2θ diffractogram. Secondly, broad bands centred approximately around the position of the others α-W reflections appear. The presence of these bands rather than sharp peaks suggests discarding the hypothesis about the formation of a solid solution of Al in W for the WAl layer. Moreover, in agreement with the findings of the θ-2θ measurements (see Fig. 3(a)), the GIXRD pattern of the W—Al layer does not show peaks related to a pure Al phase or to W—Al IMCs.

Concerning the W-800 coating, the FWHM is equal to 0.74°, corresponding to a crystallite size of about 11 nm, according to the Scherrer formula. Instead, for the WAl layer the FWHM increases to 4.7° and the crystallite size decreases to 2 nm. These values are consistent with the ones characterizing pure metallic-based amorphous films produced by PVD [49–51,62,63]. Specifically, an amorphizing effect of Al has been described in the literature for sputtered coatings based on transition metals with various composition [49–51,64–67]. Among these, the findings of *Lakdhar* et al. [49] and *Radic* et al. [50] are notable for this research. In the former work, the authors investigated DCMS co-sputtered Al-Ti-W coatings characterized by a nano-crystalline amorphous structure for various W contents (up to 17 *at.*%) and a nearly constant Ti/Al content ratio. Interestingly, all the reported Al-Ti-W films exhibited morphologies and XRD patterns very similar if compared to the W—Al layer presented in this work. Concerning W—Al films produced by conventional DCMS, the latter work demonstrated that amorphous structures could be achieved with W content in the range 20–33 *at.*%. Despite a higher W content (50 *at.*%) with respect to the two mentioned literature works, a similar amorphizing effect of Al could

hold also for the mixed coatings examined in the present study. In this regard, the HiPIMS plasma environment could have a relevant impact in the enhancement of kinetic effects at grain level triggering amorphization followed by recrystallization [68]. Thus, even in these conditions, the formation of a structure consisting in few nanometers crystal domains dispersed in an amorphous matrix can be hypothesized as suggested in [49]. This might explain the observed morphology and XRD patterns.

3.2. Short-term exposures

CuCrZr samples coated with the four W-based morphologies presented in Section 3.1 were exposed for 150 min to liquid Sn at 400 °C. Fig. 4 reports the macroscopic and microscopic inspection of the samples after the test. In the case of W-0 and W-400 coatings, once solidified the Sn drop remained firmly stuck to the samples surface (see Fig. 4(a) and (b), respectively), suggesting a significant interaction between the LM and the sample. On the other hand, as displayed in Fig. 4(c) and (d), after the end of the test the Sn drop easily detached from the sample coated with W-800 and the sample coated with the W—Al film. Specifically, in the two cases the surface region kept in contact with the LM drop can be identified by a opaque circular halo (highlighted by a red dashed circle in Fig. 4(c) and (d)). Moreover, within the interaction region, both samples exhibit relatively small darker areas distinguishing from the rest of the halo.

Concerning the last two discussed samples, the surface of the interaction region was inspected by optical microscopy and SEM. On the contrary, this characterization was not possible for pure-W samples deposited with U_S = 0 V and 400 V, since the solidified Sn droplet hindered the corroded region. The results of this analysis are presented in Fig. 4 (e-g). For both samples, the halo characterizing the interaction region is due to residual Sn nano-droplets solidified after the end of the test, as displayed in Fig. 4(e). Similar droplet formation was previously observed in fusion relevant experiment involving the use of liquid Sn [13]. On the other hand, the darker points present in the interaction region can be attributed to distinct reasons. Concerning the pure-W coating deposited with U_S = 800 V, they can be associated to corrosion spots, appearing as wrinkles and outward deformation of the coating (see Fig. 4(f)). Differently, focusing on the W—Al coated sample, the darker points are due to carbon-based impurities probably present as contaminants inside the oven (see Fig. 4(g)), while no sign of corrosion was identified.

The exposed samples were cut and prepared according to the procedure described in Section 2.2 to investigate the cross section morphology. The results related to a bare CuCrZr substrate and samples coated with W-400, W-800 and W—Al films are reported in Fig. 5. The behaviour of the W-0 coated samples is not shown since similar to the W-400 one. As shown by Fig. 5(a), the bare substrate was subjected to a uniform penetration of liquid Sn (approximately 400 μm in depth) along the entire contact area, indicating severe corrosion. The strong interaction between the LM and the CuCrZr substrate is also confirmed by a significant growth of intermetallic η and ε phases, distinguishable based on the different optical contrast in Fig. 5(b), both in the interface region and in the bulk of the Sn drop. In this respect, the Cu—Sn fraction evidenced by EDX measurements was 55–45 at.% for the η phase and 75–25 at.% for the ε phase, in agreement with literature values [57]. Concerning the W-400 coated sample, Fig. 5(c) and (d) reveal a more localized but deeper corrosion (approximately 850 μm in depth) and, as in the previous case, formation of IMCs. Consequently, the W-400 coated sample presented a corrosion depth approximately double than that of the bare substrate. This quite unintuitive behaviour can be explained by considering the saturation limit of corrosion. Assuming corrosion reached near-saturation conditions, the amount of dissolved Cu depends only on the volume of Sn present, which is constant in the two cases. Thus, corrosion depth will be inversely proportional to the exposed CuCrZr area, clearly greater for the bare substrate than for the coated one.

Notably, it can be observed that the W-400 coating, despite damaged, was not dissolved by the surrounding liquid Sn and remained semi-intact near the former Cu—Sn interface. This suggests that the inert behaviour to Sn corrosion attributed in the literature to bulk W [14,31,34] can be extrapolated to W coatings. Moreover, in Fig. 5(c) it can be observed that, after the fracture, the coating assumed a curvature compatible with an intrinsic compressive stress state, confirming the findings of XRD measurements.

Focusing on the W-800 and W—Al coated samples, cross section

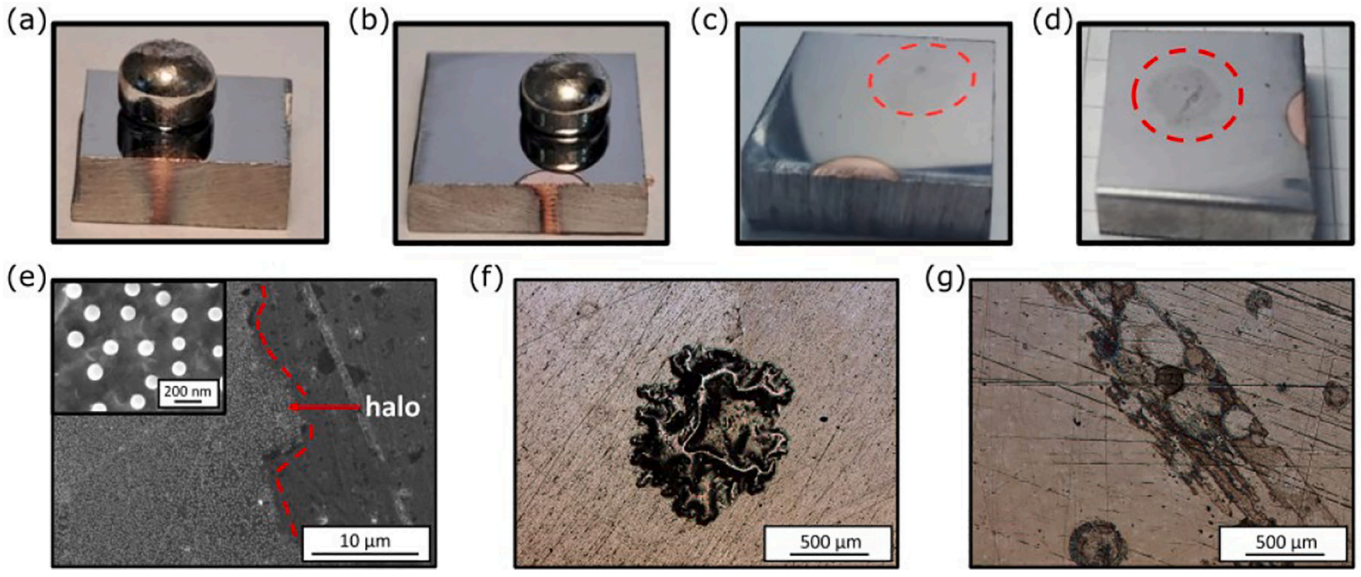

Fig. 4. Macroscopic morphologies of the pure-W coated samples deposited with (a) U_S = 0 V, (b) 400 V, and (c) 800 V and (d) W—Al coated samples after exposure to liquid Sn at 400 °C for 150 min. The red dashed circle in panels (c) and (d) approximately corresponds to the interaction region. (e) SEM planar image of the boundary between the interaction region, characterized by the presence of solidified Sn nano-droplets forming the circular"halo", and the unexposed region. The red dashed line is just a guide to the eye. Inset: magnification of the solidified Sn nano-droplets in the exposed "halo" region. Optical microscopy planar images of (f) pure-W (U_S = 800 V) and (g) W—Al coated samples after exposure to to liquid Sn for 150 min.

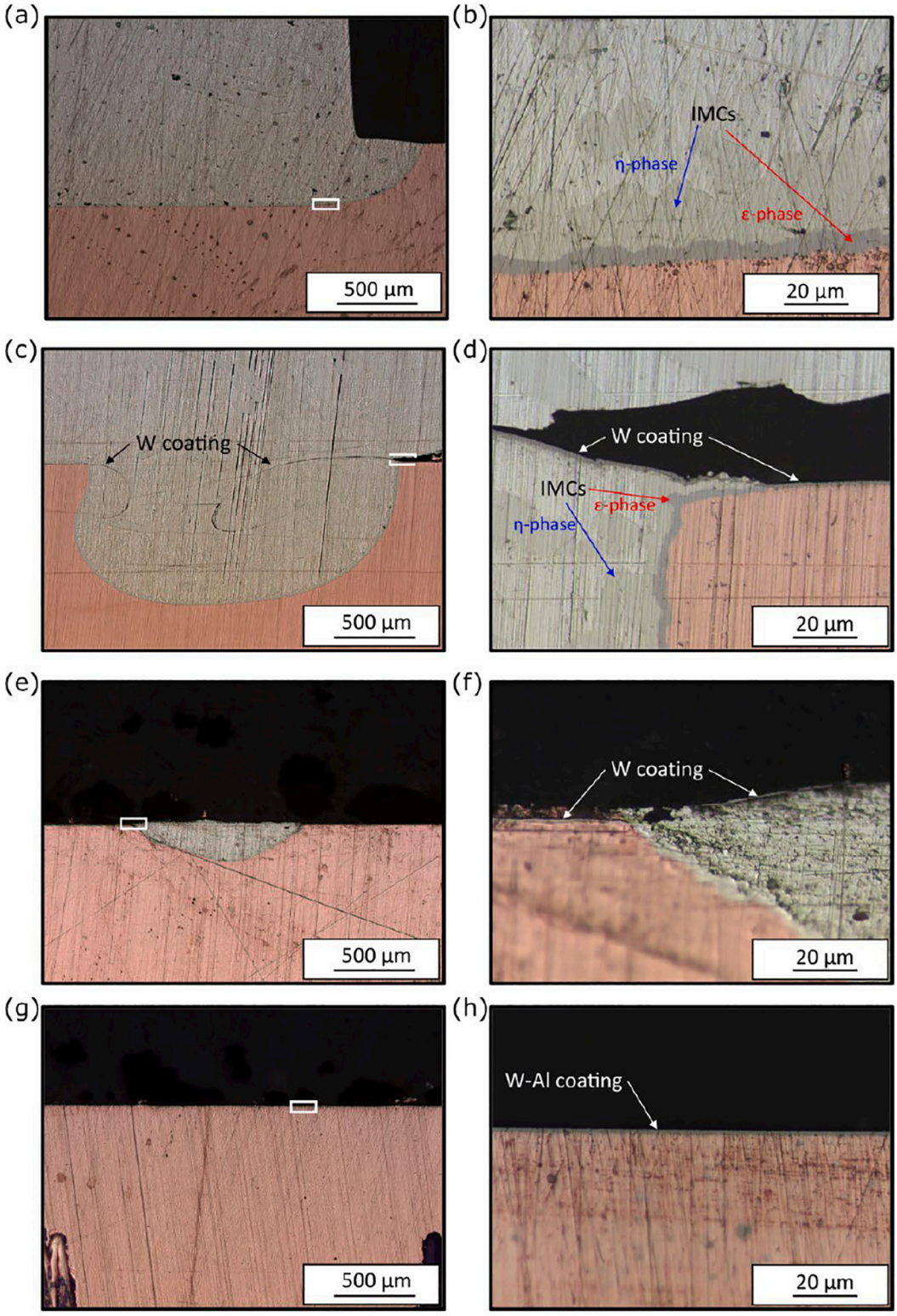

Fig. 5. Low and high magnification optical microscopy cross section images of samples exposed to liquid Sn for 150 min. The high magnification image approximately corresponds to the region delimited by the white line in the low magnification image. (a) and (b) refer to a bare CuCrZr sample. (c) and (d) refer to a sample coated with a pure-W film deposited setting $U_S = 400$ V. (e) and (f) refer to a sample coated with a pure-W film deposited setting $U_S = 800$ V. (g) and (h) refer to a sample coated with a W—Al film.

morphology corroborates the indications given by surface analysis. In the former sample, Fig. 5(e) displays a limited penetration of liquid Sn (approximately 200 µm in depth) in correspondence with the surface corrosion spot observed in the interaction region (see Fig. 4(f)). Again, in Fig. 5(f) it is possible to appreciate that the W coating is still recognizable despite corrosion started. Differently from all other tested samples, no penetration of LM was detected for the one coated with the W—Al film. Indeed, as depicted in Fig. 5(g) and (h), the cross section

morphology analysis revealed a coating-substrate interface unaltered by the contact with liquid Sn.

From the presented results it is possible to conclude that, out of the four W-based coating tested, the W-0 and W-400 ones exhibited an insufficient behaviour as barriers. Indeed, both macroscopic and microscopic analysis revealed an extensive penetration of liquid Sn through the coating and corrosive interaction with the CuCrZr substrate. Instead, better performances were observed for the W-800 and W—Al coatings. Probably, this can be related to their peculiar morphology and microstructure compared to other coatings. Indeed, as described in Section 3.1, the W-800 film was characterized by a lower crystalline degree caused by a high energy ion bombardment (U_S = 800 V), while W—Al presented a less ordered structure promoted by the co-deposition of Al. In addition, some more general considerations can be drawn. Firstly, the deep corrosion observed for the W-0 and W-400 coated samples indicates that the time duration of the test, despite shorter than the expected component lifetime, is enough to provide representative insights into the behaviour of W-based corrosion barriers. Secondly, some hints on the barrier layer failure mechanism can be drawn from the observation of the intermetallic η and ϵ phases at the interface between Cu and Sn (see Fig. 5(d) and (f)), as well as from the limited extension of the interaction area for the W-800 coated sample (about 1 mm in diameter with respect to 10 mm of interaction area, see Fig. 5(e)). Thus, corrosion starts in correspondence with coatings imperfections which constitute a preferential channel for liquid Sn penetration towards the underlying substrate. In particular, imperfections are primarily connected to the presence of unavoidable machining-related substrate defects which affect coating uniformity. In addition, the coverage of substrate irregularities can be further influenced by the specific coating growth features (e.g., a columnar morphology or a uniform amorphous-like morphology). Once in contact with liquid Sn, Cu dissolves into it reaching super-saturation and promoting nucleation of IMCs at the Sn—Cu border. The expansion caused by IMCs nucleation and growth triggers the deformation of the coating leading to its breakage. Probably, the ability of these pure-W coatings in withstanding such a dramatic variation in the film/substrate interface (from solid/solid to solid/liquid+solid) is negatively influenced also by the compressive residual stress state characterizing them, which worsen their mechanical stability after substrate dissolution. Indeed, liquid Sn starts to expand from the penetration point in all directions, leading to the dissolution of the metallic substrate (and formation of intermetallic compounds). On the contrary, the coating is not dissolved. Therefore, locally the coating freely "floats" over liquid Sn and its compressive stress state is no longer compensated by the solid CuCrZr substrate on which was originally grown. This induces the coating to curl on itself (see Fig. 6(c)) compromising its integrity and further facilitating the penetration of liquid Sn, thus leading to a positive feedback mechanism that accelerates the degradation process. Nevertheless, during the performed tests, the complete dissolution of Cu is prevented since the kinetic of the process is progressively slowed by the growth of IMCs. Lastly, as already mentioned, it is worth to highlight that, even in those cases where corrosion was observed, the coating was recognizable and not dissolved, though lifted and damaged by the expansion of IMCs. This confirms that W in the form of coatings remains inert to the aggressive liquid Sn environment, as reported for the bulk material in the literature [14,31,34].

3.3. Long-term exposures

Relying on the results presented in the previous Section, W-800 and W—Al coatings emerged as the most promising barrier materials among the ones examined. Thus, a more in-depth investigation was dedicated to these two kinds of coatings to further inspect their protective performances. The exposure time to liquid Sn was extended to 600 min. In addition, to take into account the sensitivity of corrosion experiments to defects related to substrate machining, more nominally identical samples were tested. Specifically, for each type of coating, four samples were produced to improve tests statistic and reduce the dependence on local substrate finishing.

Fig. 6 illustrates the macroscopic morphologies of W-800 and W—Al samples after the tests. As can be seen from Fig. 6(a), all the specimens coated with a pure-W layer suffered corrosion issues. In two cases (see upper part of Fig. 6(a)), the Sn drop remained stuck to the sample surface clearly indicating a corrosive interaction with the CuCrZr substrate. In the other two cases (see lower part of Fig. 6(a)), the removal of the Sn drop revealed the presence of damaged surface areas suggesting the beginning of a heavy corrosion process. On the other hand, significant differences were observed for the W—Al coatings, as shown in Fig. 6(b). The Sn drop spontaneously detached from the surface of all four samples and the coatings appeared macroscopically unaffected. Nevertheless, within the circular halo left by liquid Sn residues, it is possible to notice few points indicating a localized attack, even if to a by far lower extent compared to the W-800 samples case.

EDX analysis coupled with optical microscopy and SEM images provides further insights on the behaviour of the two tested coatings. Fig. 7 refers to a W-800 coated sample. The cross-sectional optical microscopy and SEM views show LM penetration through the W coating and the formation of IMCs both at the interface with the CuCrZr substrate and inside the Sn drop. In particular, the presence of η and ε phases is highlighted by the different contrast of the grayscale SEM image and confirmed by the EDX map which evidenced for the two phases the same compositions reported in paragraph 3.2. The latter analysis suggests that the growth of IMCs (see Fig. 7(c) and (d)) leading to the deformation and breakage of the W film is the reason behind extended corrosion, in agreement with the findings of the previous Section. Likewise, the presence of compressive stress state, which is confirmed by both the curvature of W-800 film in Fig. 7(e) and by XRD measurements, can play a role in determining the sample corrosion. Moreover, despite the longer test duration, in Fig. 7(e) the coating is still recognizable both on the substrate and inside the Sn drop. This once

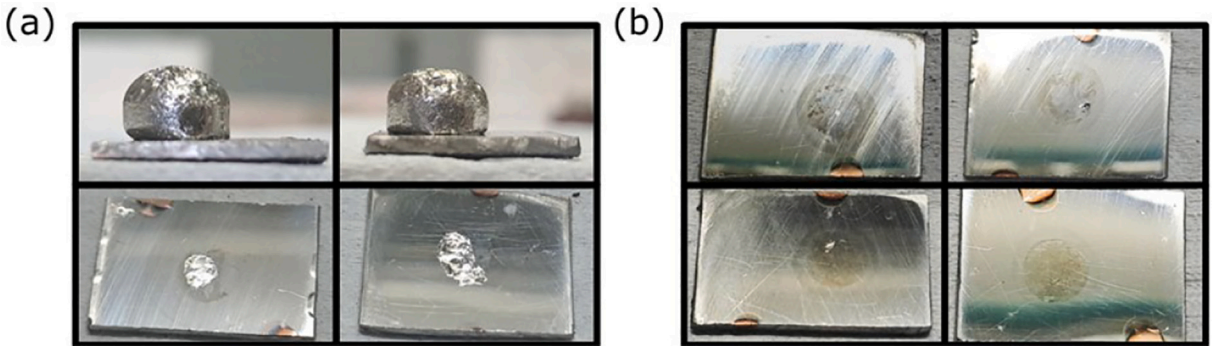

Fig. 6. Macroscopic morphologies of the (a) pure-W (U_S = 800 V) and (b) W—Al coated samples after exposure to liquid Sn at 400 °C for 600 min.

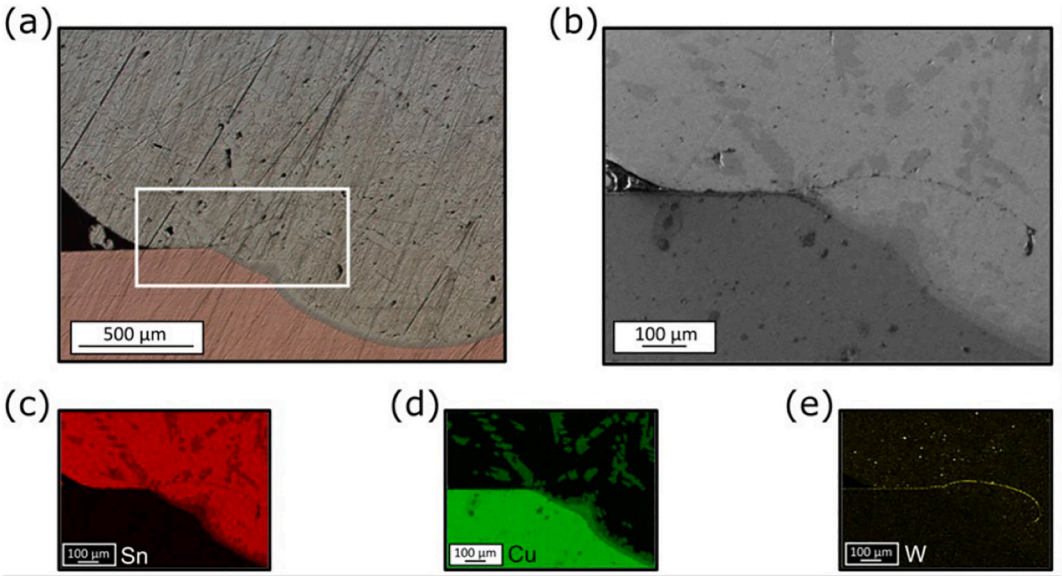

Fig. 7. (a) Optical microscopy and (b) SEM cross-sectional images of a corroded W-800 coated sample exposed to liquid Sn for 600 min. The SEM image approximately corresponds to the region delimited by the white line in the optical microscopy image. (c-e) EDX maps of a corroded W-800 coated sample. In panels (c) and (d) the formation of IMCs is evident both at the interface region and inside the Sn drop. In panel (e) the W coating can be recognized.

again demonstrates the corrosion resistance of W in liquid Sn and its potentiality as protective barrier.

Considering the W—Al coated samples, Fig. 8 shows results related to both unaffected and corroded regions. Fig. 8(a) and (b) refer to a sample in which the coating allowed to keep unaltered the underlyng CuCrZr substrate, avoiding the penetration of liquid Sn whose solid residues are visible in Fig. 8(a), (b) and (c) on top of the coating. Specifically, the addition of Al in the coating (see Fig. 8(e) and (f)) does not seem to have altered or worsened the inert behaviour in contact with liquid Sn demonstrated and observed for pure W. Fig. 8(g) and (h) refer to a W/Al sample in which liquid Sn penetration occurred. The depth and extension of corrosion are more confined with respect to the pure-W coating case. However, as can be appreciated from Fig. 8(i) and (l), the growth of IMCs at Sn/Cu interface appears more pronounced if compared to the smaller size of the affected region. Also in this case, the same compositions reported in paragraph 3.2 were retrieved by EDX measurements.

Some hypotheses can be advanced to explain the distinct evolution of corroded regions in presence of liquid Sn for the two types of coatings. In both cases, the specific coating composition is not itself the cause of corrosion, since the results of the tests suggest that, even if damaged, coatings are not dissolved in the LM. Probably, the penetration of liquid Sn is promoted in correspondence of highly irregular, but circumscribed, substrate surface regions characterized by a not optimal uniformity and quality of the coating. When the localized attack begins, the two coatings show a different behaviour with respect to the formation of IMCs. Specifically, the W-800 coating is not able to limit the action of Sn, but rather it allows a rapid expansion of the corroded region. This can be related to its morphology which, although very compact due to the application of an extremely high substrate bias voltage, could cause a brittle behaviour if subjected to external deformation. Consequently, the formation of IMCs at the boundary between substrate and coating causes the damage and breakage of the latter. In addition, the curling of the pure-W film due to its compressive stress state further increases the contact area between liquid Sn and CuCrZr. Therefore, the corrosion process is facilitated by the unhindered penetration of liquid Sn towards the substrate. The contact between a large mass of Sn and the CuCrZr substrate leads to the dissolution of a significant amount of Cu inside the LM, causing the corrosion interface to progress rapidly and the nucleation of IMCs to start even far from the interface. The thickness of IMCs therefore remains limited compared with Sn penetration depth. Indeed, due to the fast and continuous penetration of liquid Sn, IMCs have a short time available to grow at the progressing interface and their increase in size within the corroded region is relatively limited. On the contrary, the picture is different considering the W—Al coating. As assessed by morphology and XRD analysis, this coating is constituted by a central amorphous-like W—Al layer and by an external pure-W "top layer" with features similar to the one of W-800 coating. Thus, on the one hand, the latter layer guarantees the same inert behaviour shown by the pure-W coating with respect to liquid Sn. On the other hand, if corrosion starts, the peculiar microstructure of the W—Al layer could favour a more plastic and ductile response of the coating, as demonstrated in previous works related to Al—Mo alloyed films with amorphous-nanocrystalline phase [51,69]. The improved ductiliy, in turn, better mitigates the distortion caused by the IMCs formation at the substrate-coating interface. As a consequence, the more plastic behaviour could partially slow down and limit the penetration of liquid Sn. Therefore, the reduced amount of penetrating LM requires the dissolution of a smaller Cu mass to reach the supersaturation condition that triggers the growth of IMCs at the interface. This results in a larger volume occupied by IMCs within the restricted corroded area, which is an indication of how long liquid Sn remained in contact with the same Cu substrate region. Specifically, if the liquid Sn remains confined in a relatively small region of the sample for a long period, more time is available for the growth of IMCs and, as observed, they increase in size compared to the penetration depth. Thus, even in case of local failure, the characteristics of the W—Al coating allow to confine corrosion to a limited area, unlike to what happens in presence of the more crystalline pure-W coating. In this respect, an effect played by the higher thickness of W—Al coatings compared to the pure-W ones cannot be entirely excluded, but to a lower extent if compared to effects connected to morphology and microstructure differences.

4. Conclusions

This work investigated the performance of pure-W and multilayer W—Al coatings against liquid Sn corrosion under temperature conditions relevant for nuclear fusion. Specifically, coatings exhibiting different morphological and microstructural properties were obtained by exploiting different HiPIMS deposition strategies (i.e., substrate biasing and co-sputtering). In this respect, HiPIMS proved to be an

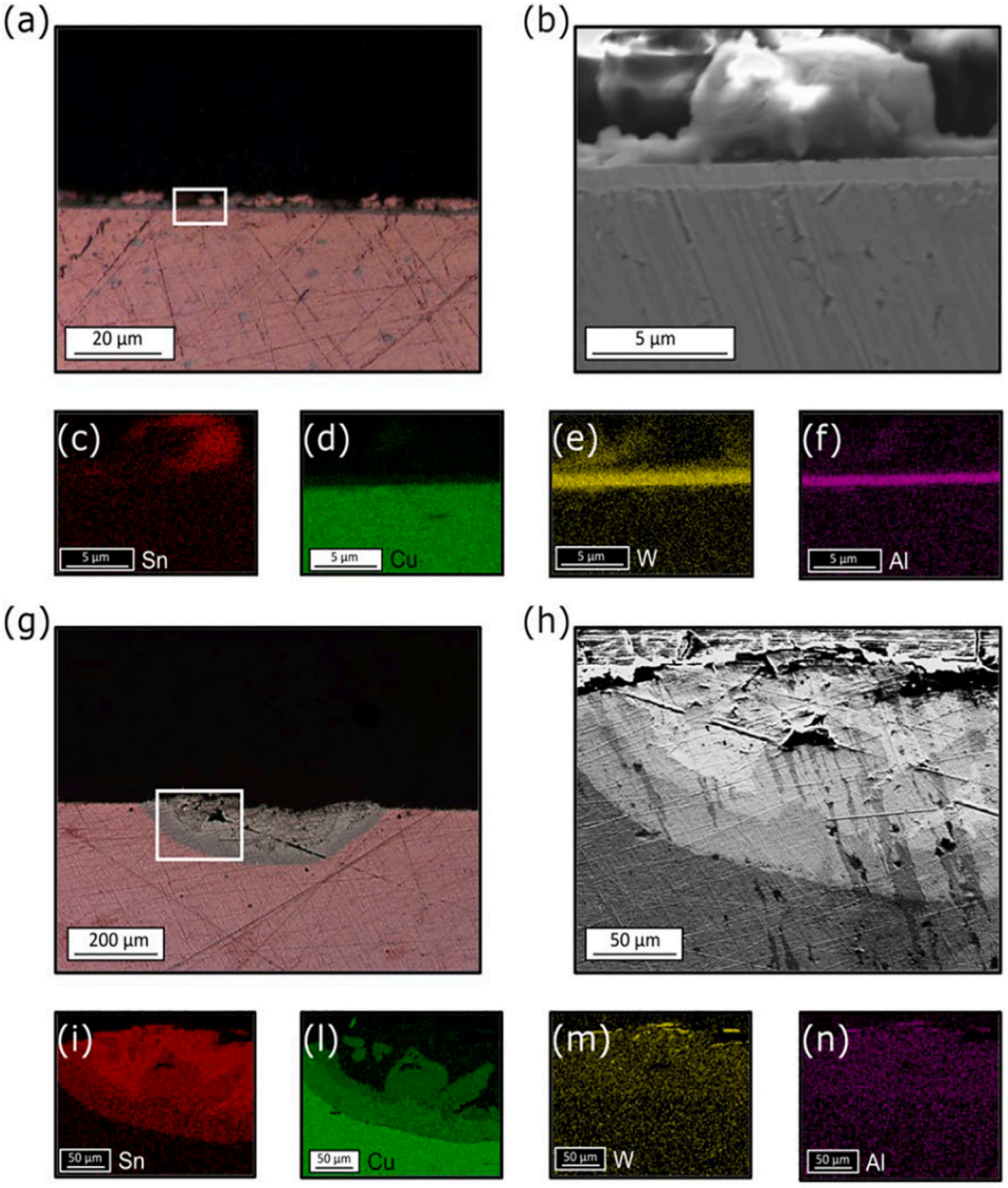

Fig. 8. (a) Optical microscopy and (b) SEM cross-sectional images of an unaltered W—Al coated sample. EDX maps (c-f) confirm that the CuCrZr substrate and liquid Sn did not interact. Specifically, in panel (b) the presence of Sn solid residues on top of the W—Al coating can be noted. In panels (e) and (f), the signals of W and Al outside the region of the coating are related to the mechanical cutting procedure performed to analyse the cross section of the sample. (g) Optical microscopy and (h) SEM cross-sectional images of a corroded W—Al coated sample. The EDX maps (i-n) allows to appreciate the size of the corroded region and the extension of IMCs. The SEM images in panels (b) and (h) approximately corresponds to the region delimited by the white line in the panels (a) and (g), respectively.

effective tool to tune W-based coatings properties down to the nanoscale. Thus, it was possible to assess not only the inertness of the produced W-based materials when in contact with liquid Sn, but also the role of different characteristics of the coatings (e.g., morphology, crystallinity) on their protective performance.

Corrosion tests were performed in the static droplet approach at a temperature of 400 °C for up to 600 min. On the one hand, all the produced W-based coatings did not exhibit a dissolution process following the interaction with liquid Sn. This suggests that an inert behaviour with respect to liquid Sn corrosion can be attributed to W-based coatings, confirming what is reported in the literature for the bulk material. On the other hand, the specific morphology and microstructure of the coatings influenced their ability to prevent liquid Sn attack towards the underlying CuCrZr substrate. Corrosion tests indicated that the most relevant failure mechanism involves irregularities in the coating surface caused by substrate roughness and defects. Indeed, once the penetration of liquid Sn started in correspondence of these limited but defective regions, the subsequent interaction with the CuCrZr substrate led to the formation and growth of Intermetallic Compounds (IMCs). The expansion of IMCs at the coating-substrate interface acted as an external deformation on the coating. This induced brittle failure on columnar pure-W coatings, facilitating liquid Sn diffusion and Cu dissolution. On the contrary, the expansion of IMCs represented a less detrimental process in the case of mixed coatings with amorphous-like features. Thus, they were able to limit corrosion to a confined region of the sample, while leaving unaltered most of the surface interaction area. These results allow to conclude that while all the W-based coatings exhibit an inert behaviour with respect to liquid Sn interaction, the

specific film characteristics obtained by HiPIMS majorly influence their barrier effectiveness. Notably, among the types of films investigated in this work, corrosion tests evidence the superior performances of the engineered W—Al multilayer coating, which represents a promising candidate to protect CuCrZr components from liquid Sn corrosion in future liquid metal divertor concepts. Based on these observations, the research activity should continue in a twofold direction. Concerning coatings characterization, the connection between mechanical properties and the observed protective behaviour must be investigated. Additionally, since surface imperfections will be unavoidable in a realistic component, the role of substrate roughness and coating thickness must be addressed in future corrosion experiments.

CRediT authorship contribution statement

D. Vavassori: Writing – review & editing, Writing – original draft, Visualization, Methodology, Investigation, Formal analysis. **L. Bana:** Writing – review & editing, Writing – original draft, Visualization, Investigation, Formal analysis. **M. Bugatti:** Writing – original draft, Investigation, Formal analysis. **G. Marra:** Investigation. **V. Pinto:** Investigation. **D. Dellasega:** Writing – review & editing, Supervision, Formal analysis. **M. Iafrati:** Writing – review & editing, Methodology, Conceptualization. **M. Passoni:** Writing – review & editing, Supervision, Funding acquisition.

Declaration of competing interest

The authors declare the following financial interests/personal relationships which may be considered as potential competing interests: Matteo Passoni reports financial support was provided by European Consortium for the Development of Fusion Energy. Luigi Bana reports financial support was provided by Eni SpA. If there are other authors, they declare that they have no known competing financial interests or personal relationships that could have appeared to influence the work reported in this paper.

Acknowledgements

This work has been carried out within the framework of the EUROfusion Consortium, funded by the European Union via the Euratom Research and Training Programme (Grant Agreement No 101052200 — EUROfusion). Views and opinions expressed are however those of the author(s) only and do not necessarily reflect those of the European Union or the European Commission. Neither the European Union nor the European Commission can be held responsible for them. L. B. acknowledges Eni S.p.A. for funding his PhD program.

Appendix A. Supplementary data

Supplementary data to this article can be found online at https://doi.org/10.1016/j.surfcoat.2024.131449.

Data availability

The data supporting the findings of this work are available from the corresponding authors upon reasonable request.

References

[1] J. Zhang, Liquid Metal Corrosion: Fundamental Theory and Applications, Elsevier, 2023, https://doi.org/10.1016/C2021-0-00403-X.
[2] Y. Deng, J. Liu, Liquid Metals for Advanced Energy Applications, AIP Publishing LLC, 2022, https://doi.org/10.1063/9780735424791.
[3] T. Gnanasekaran, Science and Technology of Liquid Metal Coolants in Nuclear Engineering, Woodhead Publishing, 2022, https://doi.org/10.1016/C2021-0-02128-3.
[4] P. Lorusso, et al., GEN-IV LFR development: status & perspectives, Prog. Nucl. Energy 105 (2018) 318–331, https://doi.org/10.1016/j.pnucene.2018.02.005, issn: 0149-1970.
[5] R. Nygren, F. Tabar'es, Liquid surfaces for fusion plasma facing components—a critical review. Part I: Physics and PSI, Nuclear Materials and Energy 9 (2016) 6–21, https://doi.org/10.1016/j.nme.2016.08.008, issn: 2352–1791.
[6] C.E. Kessel, et al., Critical exploration of liquid metal plasma-facing components in a fusion nuclear science facility, Fusion Sci. Technol. 75 (8) (2019) 886–917, https://doi.org/10.1080/15361055.2019.1610685.
[7] C.F. Smith, L. Cinotti, Lead-cooled Fast Reactors (LFRs), in: I.L. Pioro (Ed.), Handbook of Generation IV Nuclear Reactors, ser. Woodhead Publishing Series in Energy, Second edition, Woodhead Publishing, 2023, pp. 195–230, isbn: 978-0-12-820588-4. doi:10.1016/B978-012-820588-4.00018-9.
[8] T.W. Morgan, P. Rindt, G.G. van Eden, V. Kvon, M.A. Jaworksi, N.J.L. Cardozo, Liquid metals as a divertor plasma-facing material explored using the pilot-PSI and MagnumPSI linear devices, Plasma Phys. Controlled Fusion 60 (1) (2017) 014025, https://doi.org/10.1088/1361-6587/aa86cd.
[9] P. Rindt, J. van den Eijnden, T. Morgan, N. Lopes Cardozo, Conceptual design of a liquidmetal divertor for the European DEMO, Fusion Engineering and Design 173 (2021) 112812, https://doi.org/10.1016/j.fusengdes.2021.112812, issn: 0920-3796.
[10] S. Roccella, G. Dose, R. de Luca, M. Iafrati, A. Mancini, G. Mazzitelli, CPS based liquid metal Divertor target for EU-DEMO, J. Fusion Energ. 39 (6) (2020) 462–468, https://doi.org/10.1007/s10894-020-00263-4.
[11] R.A. Pitts, et al., Physics basis for the first ITER tungsten divertor, Nuclear Materials and Energy 20 (2019) 100696, https://doi.org/10.1016/j.nme.2019.100696.
[12] C. Linsmeier, et al., Development of advanced high heat flux and plasma-facing materials, Nuclear Fusion 57 (9) (2017) 092007, https://doi.org/10.1088/1741-4326/aa6f71.
[13] J.G.A. Scholte, et al., Reducing tin droplet ejection from capillary porous structures under hydrogen plasma exposure in magnum-PSI, Nuclear Materials and Energy 34 (Mar. 2023) 101315, https://doi.org/10.1016/j.nme.2022.101315, issn: 2352-1791.
[14] A. Vertkov, I. Lyublinski, M. Zharkov, G. Mazzitelli, M. Apicella, M. Iafrati, Liquid tin limiter for FTU tokamak, Fusion Engineering and Design 117 (2017) 130–134, https://doi.org/10.1016/j.fusengdes.2017.01.041.
[15] G. Nallo, G. Mazzitelli, M. Moscheni, F. Subba, R. Zanino, SOLPS-ITER simulations of a CPS-based liquid metal divertor for the EU DEMO: Li vs Sn, Nucl. Fusion 62 (3) (2022) 036008, https://doi.org/10.1088/1741-4326/ac4867.
[16] I. Kawakatsu, T. Osawa, Wettability of liquid tin on solid copper, Trans. Jpn. Inst. Metals 14 (2) (1973) 114–119, https://doi.org/10.2320/matertrans1960. 14.114.
[17] R.A. Gagliano, G. Ghosh, M.E. Fine, Nucleation kinetics of Cu6Sn5 by reaction of molten tin with a copper substrate, J. Electron. Mater. 31 (11) (Nov. 2002) 1195–1202, https://doi.org/10.1007/s11664-002-0010-1, issn: 1543-186X.
[18] O. Liashenko, A.M. Gusak, F. Hodaj, Phase growth competition in solid/liquid reactions between copper or Cu3Sn compound and liquid tin-based solder, J. Mater. Sci. Mater. Electron. 25 (10) (Oct. 2014) 4664–4672, https://doi.org/10.1007/s10854-014-2221-7, issn: 1573-482X.
[19] A. Hayashi, C. Kao, Y. Chang, Reactions of solid copper with pure liquid tin and liquid tin saturated with copper, Scr. Mater. 37 (4) (1997) 393–398, https://doi.org/10.1016/S1359-6462(97)00129-2.
[20] L. Snugovsky, M.A. Ruggiero, D.D. Perovic, J.W. Rutter, Experiments on interaction of liquid tin with solid copper, Mater. Sci. Technol. 19 (7) (2003) 866–874, https://doi.org/10.1179/026708303225002794.
[21] M.A.A. Mohd Salleh, S.D. McDonald, H. Yasuda, A. Sugiyama, K. Nogita, Rapid Cu6Sn5 growth at liquid Sn/solid cu interfaces, Scr. Mater. 100 (2015) 17–20, https://doi.org/10.1016/j.scriptamat.2014.11.039.
[22] J. Saito, Y. Kobayashi, H. Shibutani, Wettability of pure metals with liquid sodium and liquid tin, Mater. Trans. 62 (10) (2021) 1524–1532, https://doi.org/10.2320/matertrans.MT-M2021107.
[23] N. Zaho, Y. Zhong, M.L. Huang, H.T. Ma, W. Dong, Growth kinetics of Cu6Sn5 intermetallic compound at liquid-solid interfaces in cu/Sn/cu interconnects under temperature gradient, Sci. Rep. 5 (13491) (2015), https://doi.org/10.1038/srep13491.
[24] W. Zhang, et al., Screening of the FeCrAl LBE corrosion-resistant coatings: the effect of Cr and Al contents, Surf. Coat. Technol. 462 (2023) 129477, https://doi.org/10.1016/j.surfcoat.2023.129477, issn: 0257-8972.
[25] E. Miorin, et al., Al rich PVD protective coatings: a promising approach to prevent T91 steel corrosion in stagnant liquid lead, Surf. Coat. Technol. 377 (2019) 124890, https://doi.org/10.1016/j.surfcoat.2019.124890.
[26] J. Yang, et al., Influence of coating thickness on microstructure, mechanical and LBE corrosion performance of amorphous AlCrFeTiNb high-entropy alloy coatings, Surf. Coat. Technol. 441 (2022) 128502, https://doi.org/10.1016/j.surfcoat.2022.128502, issn: 0257-8972.
[27] H. Shi, et al., Corrosion behavior of Al-containing MAX-phase coatings exposed to oxygen containing molten Pb at 600 C, Corros. Sci. 201 (2022) 110275, https://doi.org/10.1016/j.corsci.2022.110275, issn: 0010938X.
[28] F.G. Ferré, et al., Corrosion and radiation resistant nanoceramic coatings for lead fast reactors, Corros. Sci. 124 (2017) 80–92, https://doi.org/10.1016/j.corsci.2017.05.011.
[29] E. Serag, B. Caers, P. Schuurmans, S. Lucas, E. Haye, Challenges and coating solutions for wear and corrosion inside Lead bismuth eutectic: a review, Surf. Coat. Technol. 441 (2022) 128542, https://doi.org/10.1016/j.surfcoat.2022.128542.

[30] M. Kondo, M. Yukihiro, Y. Kitamura, M. O., T. Tanaka, Corrosion mechanism of reduced activation ferritic martensitic steel JLF-1 in liquid metal Sn, Corros. Sci. 209 (2022) 110748, https://doi.org/10.1016/j.corsci.2022.110748.
[31] L.R. Kelman, W.D. Wilkinson, F.L. Yaggee, Resistance of materials to attack by liquid metals, Argonne National Laboratory 150 (1950) no. ANL-4417. doi: 10.2172/4419134.
[32] Y. Zhang, et al., Containment materials for liquid tin at 1350 C as a heat transfer fluid for high temperature concentrated solar power, Sol. Energy 164 (2018) 47–57, https://doi.org/10.1016/j.solener.2018.01.085, issn: 0038-092X.
[33] M. Kondo, M. Tada, Y. Ohtsuka, Y. Hishinuma, T. Muroga, Corrosion resistance of Al-rich steel and Al2O3 ceramic bulk in liquid Sn, Fusion Eng. Des. 146 (2019) 2450–2456, https://doi.org/10.1016/j.fusengdes.2019.04.016.
[34] N. Kawano, Y. Tamai, M. Kondo, Excellent corrosion resistance of tungsten materials in liquid tin, Plasma and Fusion Research 15 (2020) 1205068, https://doi.org/10.1585/pfr.15.1205068.
[35] M. Kondo, et al., Conceptual design of HFIR irradiation experiment for material compatibility study on liquid Sn divertor, Plasma and Fusion Research 16 (2021) 2405040.
[36] I. Tazhibayeva, et al., Study of liquid tin-lithium alloy interaction with structural materials of fusion reactor at high temperatures, Nuclear Materials and Energy 30 (2022) 101152, https://doi.org/10.1016/j.nme.2022.101152.
[37] O.V. Ogorodnikova, et al., Deuterium retention in dense and disordered nanostructured tungsten coatings, J. Nucl. Mater. 507 (2018) 226–240, https://doi.org/10.1016/j.jnucmat.2018.04.039, issn: 00223115.
[38] S. Brezinsek et al., "Surface Modification of He Pre-Exposed Tungsten Samples by He Plasma Impact in the Divertor Manipulator of ASDEX Upgrade," Nuclear Materials and Energy, Proceedings of the 22nd International Conference on Plasma Surface Interactions 2016, 22nd PSI, vol. 12, pp. 575–581, 2017, issn: 2352-1791. doi:https://doi.org/10.1016/j.nme.2016.11.002.
[39] M. Reinhart et al., "Latest Results of Eurofusion Plasma-Facing Components Research in the Areas of Power Loading, Material Erosion and Fuel Retention," Nuclear Fusion, vol. 62, no. 4, p. 042013, 2022, issn: 0029–5515, 1741–4326. doi: https://doi.org/10.1088/1741-4326/ac2a6a.
[40] A. Bigos, F. Valenza, P. Czaja, I. Kwiecien, J. Wojewoda-Budka, Interface reaction between tin solder and Nanocrystalline Ni and Ni-Mo coatings obtained by electrodeposition, Journal of Materials Engineering and Performance 31 (9) (2022) 7061–7067, https://doi.org/10.1007/s11665-022-06840-2.
[41] D. Lundin, J.T. Gudmundsson, T. Minea, High power impulse magnetron sputtering: fundamentals, technologies, challenges and applications, Elsevier (2020), https://doi.org/10.1016/C2016-0-02463-4 isbn: 9780128124543.
[42] F. Cemin, et al., Benefits of energetic ion bombardment for tailoring stress and microstructural evolution during growth of cu thin films, Acta Mater. 141 (2017) 120–130, https://doi.org/10.1016/j.actamat.2017.09.007, issn: 1359-6454.
[43] D. Dellasega, F. Mirani, D. Vavassori, C. Conti, M. Passoni, Role of energetic ions in the growth of fcc and ω crystalline phases in Ti films deposited by HiPIMS, Appl. Surf. Sci. 556 (2021) 149678, https://doi.org/10.1016/j.apsusc.2021.149678, issn: 0169-4332.
[44] R.P.B. Viloan, U. Helmersson, D. Lundin, Copper thin films deposited using different ion acceleration strategies in HiPIMS, Surf. Coat. Technol. 422 (2021) 127487, https://doi.org/10.1016/j.surfcoat.2021.127487, issn: 0257-8972.
[45] I.L. Velicu, et al., Enhanced properties of tungsten thin films deposited with a novel HiPIMS approach, Appl. Surf. Sci. 424 (2017) 397–406, https://doi.org/10.1016/j.apsusc.2017.01.067, issn: 0169-4332.
[46] A.M. Engwall, S.J. Shin, J. Bae, Y.M. Wang, Enhanced properties of tungsten films by high-power impulse magnetron sputtering, Surf. Coat. Technol. 363 (2019) 191–197, https://doi.org/10.1016/j.surfcoat.2019.02.055, issn: 0257-8972.
[47] T. Shimizu, et al., Low temperature growth of stress-free single phase α-W films using HiPIMS with synchronized pulsed substrate bias, J. Appl. Phys. 129 (15) (2021) 155305, https://doi.org/10.1063/5.0042608.
[48] D. Vavassori, F. Mirani, F. Gatti, D. Dellasega, M. Passoni, Role of magnetic field and bias configuration on HiPIMS deposition of W films, Surf. Coat. Technol. 458 (2023) 129343, https://doi.org/10.1016/j.surfcoat.2023.129343, issn: 0257-8972.
[49] I. Lakdhar, A. Alhussein, J. Capelle, J. Creus, Al-Ti-W alloys deposited by magnetron sputtering: effective barrier to prevent steel hydrogen embrittlement, Appl. Surf. Sci. 567 (2021) 150786, https://doi.org/10.1016/j.apsusc.2021.150786.
[50] N. Radi'c, A. Tonejc, M. Milun, P. Pervan, J. Ivkov, M. Stubǐcar, Preparation and structure of AlW thin films, Thin Solid Films 317 (1) (1998) 96–99, https://doi.org/10.1016/S0040-6090(97)00508-7, issn: 0040-6090.
[51] C. Wang, T. Wang, L. Cao, G. Wang, G. Zhang, Solid solution or amorphous phase formation in Al-Mo alloyed films and their mechanical properties, J. Alloys Compd. 746 (2018) 77–83, https://doi.org/10.1016/j.jallcom.2018.02.230.
[52] H. Yan, W. Zhang, F. Qian, P. Guo, Q. Wang, C. Zhao, Wettability and thermal performance of Ga62.5In21.5Sn16 liquid metal alloy on W-coated cu substrates with varying film thickness, Int. J. Therm. Sci. 172 (2022) 107333, https://doi.org/10.1016/j.ijthermalsci.2021.107333, issn: 1290-0729.
[53] T. Gancarz, et al., The interfacial phenomena between graphene on cu substrate covered by Ni, cu, or W layer, with liquid Ga-Sn-Zn alloy, J. Mater. Eng. Perform. (2023) 1–7, https://doi.org/10.1007/s11665-023-08022-0.
[54] Y. Cui, et al., Liquid metal corrosion effects on conventional metallic alloys exposed to eutectic gallium–indium alloy under various temperature states, Int. J. Thermophys. 39 (2018) 1–14, https://doi.org/10.1007/s10765-018-2440-x.
[55] A. Ramos-Masana, C. Colominas, Evaluation of DC-MS and HiPIMS TiB2 and TaN coatings as diffusion barriers against molten aluminum: an insight into the wetting mechanism, Surf. Coat. Technol. 375 (2019) 171–181, https://doi.org/10.1016/j.surfcoat. 2019.06.031.
[56] S. Handschuh-Wang, et al., Corrosion-resistant functional diamond coatings for reliable interfacing of liquid metals with solid metals, ACS Appl. Mater. Interfaces 12 (36) (2020) 40891–40900, https://doi.org/10.1021/acsami.0c09428.
[57] S. Furtauer, D. Li, D. Cupid, H. Flandorfer, The Cu–Sn phase diagram, Part I: new experimental results, Intermetallics 34 (2013) 142–147, doi:10.1016/j.intermet.2012.10.004.
[58] N. Brenning, J.T. Gudmundsson, M.A. Raadu, T.J. Petty, T. Minea, D. Lundin, A unified treatment of self-sputtering, process gas recycling, and runaway for high power impulse sputtering magnetrons, Plasma Sources Science and Technology 26 (12) (2017), https://doi.org/10.1088/1361-6595/aa959b, p. 125003. issn: 0963-0252.
[59] M. Ghidelli, et al., Size-dependent failure mechanisms in ZrNi thin metallic glass films, Scr. Mater. 89 (2014) 9–12, https://doi.org/10.1016/j.scriptamat.2014.06.011.
[60] M. Ghidelli, et al., Extrinsic mechanical size effects in thin ZrNi metallic glass films, Acta Mater. 90 (2015) 232–241, https://doi.org/10.1016/j.actamat.2015.02.038.
[61] P. Wang, et al., Thermodynamic re-assessment of the Al-co-W system, Calphad 59 (2017) 112–130, https://doi.org/10.1016/j.calphad.2017.09.007.
[62] D. Dellasega, G. Merlo, C. Conti, C.E. Bottani, M. Passoni, Nanostructured and amorphous-like tungsten films grown by pulsed laser deposition, J. Appl. Phys. 112 (8) (2012) 084328, https://doi.org/10.1063/1.4761842.
[63] B. Braeckman, D. Depla, On the amorphous nature of sputtered thin film alloys, Acta Mater. 109 (2016) 323–329, https://doi.org/10.1016/j.actamat.2016.02.035.
[64] E. Akiyama, A. Kawashima, K. Asami, K. Hashimoto, The corrosion behavior of sputter-deposited amorphous Al Cr Mo alloys in 1 M HCl, Corros. Sci. 38 (2) (1996) 279–292, https://doi.org/10.1016/0010-938X(96)00119-9, issn: 0010-938X.
[65] P.J. Su, C.K. Chung, Amorphization of Ta-Al films using magnetron sputtering, Surface and Coatings Technology, ICMCTF 200 (5) (2005) 1664–1668, https://doi.org/10.1016/j.surfcoat.2005.08.100, issn: 0257-8972.
[66] F. Sanchette, A. Billard, Main features of magnetron sputtered aluminium–transition metal alloy coatings, in: Surface and Coatings Technology, Proceedings of the 7th International Conference on Plasma Surface Engineering vol. 142–144, 2001, pp. 218–224, https://doi.org/10.1016/S0257-8972(01)01197-5, issn: 02578972.
[67] B.R. Braeckman, et al., High entropy alloy thin films deposited by magnetron sputtering of powder targets, Thin Solid Films 580 (2015) 71–76, issn: 0040-6090. doi:10. 1016/j.tsf.2015.02.070.
[68] M. Kateb, H. Hajihoseini, J.T. Gudmundsson, S. Ingvarsson, Role of ionization fraction on the surface roughness, density, and interface mixing of the films deposited by thermal evaporation, dc magnetron sputtering, and HiPIMS: an atomistic simulation, J. Vac. Sci. Technol. A 37 (3) (2019) 031306, https://doi.org/10.1116/1.5094429.
[69] C. Wang, T. Wang, B. Li, S. Yu, L. Cao, G. Zhang, Improving ductility of Al 0.74Mo0.26 alloy films through synergy of phase fraction and morphology of nanocrystallites dispersed in amorphous matrix, Material Science & Engineering A 799 (2021) 140146, https://doi.org/10.1016/j.msea.2020.140146.